DALTON
FULL PAPER

Biologically inspired polyoxometalate–surfactant composite materials. Investigations on the structures of discrete, surfactant-encapsulated clusters, monolayers, and Langmuir–Blodgett films of $(DODA)_{40}(NH_4)_2[(H_2O)_n \subset Mo_{132}O_{372}(CH_3CO_2)_{30}(H_2O)_{72}]$†

Dirk G. Kurth,*[a] Pit Lehmann,[a] Dirk Volkmer,*[b] Achim Müller[b] and Dietmar Schwahn[c]

[a] *Max-Planck-Institute of Colloids and Interfaces, D-14424 Potsdam, Germany. E-mail: Kurth@mpikg-golm.mpg.de; Fax: +49 (0)331/567-9202*
[b] *Department of Chemistry, AC 1, University of Bielefeld, PO Box 100 131, D-33501 Bielefeld, Germany. E-mail: dirk.volkmer@uni-bielefeld.de; Fax: +49 (0)521/106-6003*
[c] *Institut für Festkörperforschung (IFF), Forschungszentrum Jülich GmbH, D-52425 Jülich, Germany*

Received 26th April 2000, Accepted 22nd June 2000
First published as an Advance Article on the web 9th October 2000

A detailed analysis of the supramolecular architecture of the nanoporous surfactant-encapsulated cluster (SEC) with the empirical formula $(DODA)_{40}(NH_4)_2[(H_2O)_n \subset Mo_{132}O_{372}(CH_3CO_2)_{30}(H_2O)_{72}]$ **1** ($n \approx 50$) is presented. The open framework architecture of the Keplerate cluster is investigated by means of small angle neutron scattering (SANS) in $CDCl_3$ solutions containing discrete SECs. A simplifying core–shell model of **1** is developed, which describes the SEC as a solvent-filled nanocavity, surrounded by two concentric shells (a first polyoxometalate shell of 2.96 nm outer diameter, and a consecutive surfactant shell of 6.18 nm outer diameter, respectively). The model is successfully applied to probe the content of H_2O/D_2O guest molecules in the Keplerate host. Different surface analytical techniques are applied to characterize the hierarchical structures of monolayers and thin films of **1**. Monolayers at the air–water interface are investigated by means of optical ellipsometry and Brewster angle microscopy. Electron density profiles of the monolayers of **1** are gained from synchrotron X-ray reflectance (XRR) measurements that provide further evidence for the supramolecular core-shell architecture of the SEC. Within the spatial resolution limits of these analytical methods, the current data support a monolayer model consisting of hexagonal close-packed arrays of discrete SECs, floating at the air–water interface. Langmuir–Blodgett (LB) transfer of compressed monolayers on to a solid substrate leads to homogeneous multilayers. In the XRR spectra of LB multilayers of **1** multiple Bragg reflections appear, thus indicating an intrinsic tendency of the SECs to adapt a 3-dimensional, highly ordered solid state structure. Considering the huge variety of structurally different polyoxometalates and the possibility to tailor the surfactant shell by means of classic organic synthesis, the self-organization of hierarchically structured thin films and solids based on SECs bears promising perspectives towards the engineering of functional materials.

Introduction

Transition metal polyoxometalates (POMs) represent an important class of inorganic clusters,[1] with many applications in science and technology such as catalysis,[2] electrochemistry,[3] electrooptics,[4] medicine,[5] corrosion protection, dyes/pigments, dopants in (non-)conductive polymers, dopants in sol–gel matrixes, bleaching of paper pulp, and analytical chemistry.[6] The rational design of POM multi-component materials with well defined supramolecular architectures represents the next milestone to implement POMs into functional materials and devices. Our approach towards this goal is based on modifying the POM surface with surfactants, yielding discrete *surfactant-encapsulated clusters* (SECs). While the so-called "membrane mimetic"[7] approach has been successfully used in the past to stabilize a variety of semiconductor and precious metal nanoparticles,[8] it has never been applied convincingly to POM chemistry for the purpose of producing discrete monodisperse cluster species.[9]

Our motivation to use SECs rather than "naked" POM clusters has the following rationale: the surfactant shell improves the *stability* of the encapsulated cluster against *fragmentation*, enhances the *solubility* of the encapsulated clusters in non-polar, aprotic organic solvents, neutralizes the *charge* of the anionic POM, thus leading to discrete, *electrostatically neutral* assemblies, and alters the *surface chemical properties* of the POM (*e.g.* self-aggregation, surface adhesion, wetting behavior) in a predictable manner. A "program" of (inter-)molecular interactions can thus be employed to build up the supramolecular architecture of SEC-based materials on several length scales: at the atomic level, POM self-assembly proceeds by linking together low-molecular metal–oxygen building blocks of different sizes and shapes. The design of POM compounds based on virtual libraries of M–O building blocks has approached a high degree of sophistication, resulting for instance in the directed synthesis of inorganic superfullerenes and giant ring-shaped polyoxomolybdates with nanosized cavities.[10] At the nanoscopic structural level, self-assembly of surfactants and POMs leads to discrete SECs possessing a core–shell structure with a chemically well defined composition. Auto-assembly of SECs at the air–water interface

† Based on the presentation given at Dalton Discussion No. 3, 9–11th September 2000, University of Bologna, Italy.

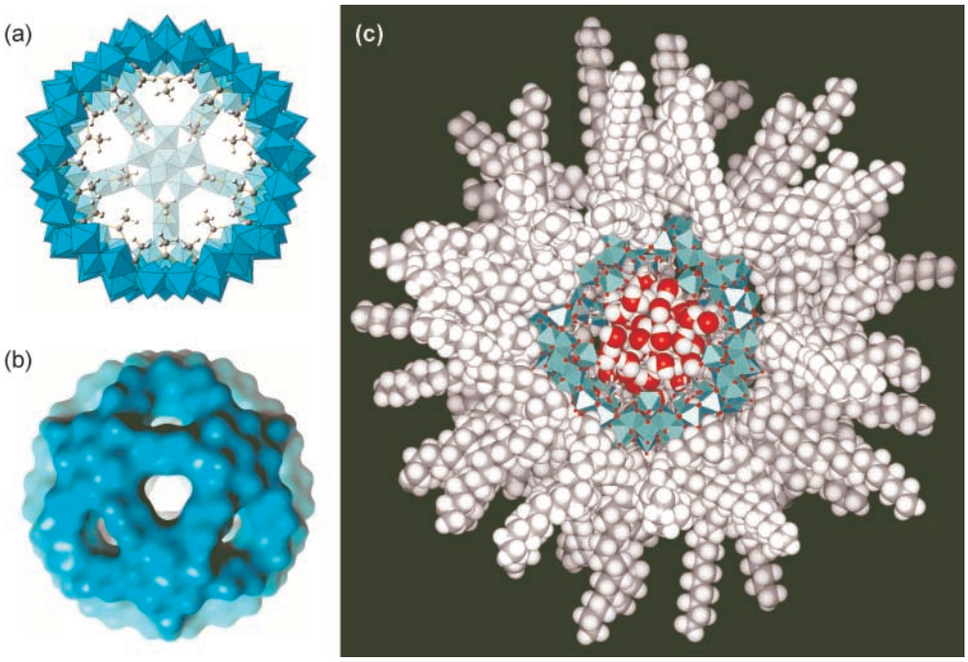

Fig. 1 Different representations of the surfactant-encapsulated cluster (SEC) $(DODA)_{40}(NH_4)_2[(H_2O)_{50} \subset Mo_{132}O_{372}(CH_3CO_2)_{30}(H_2O)_{72}]$, **1**. (a) Mo–O polyhedra model of the Keplerate $[(H_2O)_{50} \subset Mo_{132}O_{372}(CH_3CO_2)_{30}(H_2O)_{72}]^{42-}$ viewed in cross-section; acetate ligands are drawn in ball-and-stick representation. (b) Solvent-accessible surface of the Keplerate cluster, calculated for a 0.14 nm surface probe (= Connolly surface). (c) Snapshot taken from an MD simulation (MM+ force field) of **1**. H_2O molecules hosted in the nanocavity and DODA surfactants are drawn as CPK (Corey–Pauling–Koltun) models, while the Keplerate is displayed as polyhedra model. (A few surfactants and a fraction of the cluster have been omitted in order to produce a pseudo cross-sectional view of the SEC.)

or on solid supports finally results in two- or three-dimensional periodic arrangements, extending into macroscopic dimensions. We conclude that POM self-encapsulation bears the potential of a powerful, yet facile method to produce two- and three-dimensional hierarchically structured materials.[11]

In contrast with the simplicity of SEC fabrication, the *characterization* of the internal supramolecular architecture of SEC thin films and materials, which spans several length scales, often develops into a rather demanding task, requiring a multitude of complementary analytical techniques. In a previous publication[12] we have described the preparation and selected structural properties of a particular SEC, namely the compound $(DODA)_{40}(NH_4)_2[(H_2O)_n \subset Mo_{132}O_{372}(CH_3CO_2)_{30}(H_2O)_{72}]$ **1** (DODA = dimethyldioctadecylammonium, $n \approx 50$); Fig. 1 summarizes the most important features of the discrete, surfactant-encapsulated nanoporous Keplerate cluster. Structural details of **1** are based on current TEM and small angle X-ray scattering (SAXS) investigations, as well as on the X-ray crystallographic characterization of Keplerate clusters,[13] that are further accomplished here by results gained from analytical ultracentrifugation (AUC), SANS (small angle neutron scattering), and IR investigations. We will focus our attention on the characterization of SEC monolayers and thin films. Monolayers at the air–water interface are investigated by means of optical ellipsometry and Brewster angle microscopy (BAM), while synchrotron X-ray reflectance (XRR) measurements provide the electron density profile of monolayers of **1**. Langmuir–Blodgett (LB) film transfer of compressed monolayers on to solid substrates leads to homogeneous multilayers of **1** that are characterized by XRR spectroscopy and optical techniques.

Experimental

The compound $(DODA)_{40}(NH_4)_2[(H_2O)_n \subset Mo_{132}O_{372}(CH_3CO_2)_{30}(H_2O)_{72}]$ **1** ($n \approx 50$) was synthesized according to a previously published procedure.[12] Details for the analytical ultracentrifugation measurements, for the preparation of Langmuir and LB films, as well as for experimental procedures of BAM and XRR measurements are given in ref. 11.

Small angle neutron scattering

For SANS investigations two different samples of **1** were prepared. Compound **1(D_2O)** was prepared by dissolving a sample of the starting compound $(NH_4)_{42}[(H_2O)_{50} \subset Mo_{132}O_{372}(CH_3CO_2)_{30}(H_2O)_{72}]$·*ca.* 250 H_2O·*ca.* 10 $CH_3CO_2NH_4$ (286 mg, 0.01 mmol) in D_2O (5 mL). The solution was stirred for 2 h under ambient conditions in order to allow D_2O exchange of H_2O guest molecules (or co-ordinated H_2O) that are located within the nanocavity of the Keplerate cluster. As a reference sample, an equal amount of the starting compound was dissolved in 5 mL of water. Both solutions were equally treated with $CHCl_3$ solutions containing dimethyldioctadecylammonium bromide [DODA]Br at the appropriate stoichiometric ratio (42 : 1). The $CHCl_3$ solution of **1(D_2O)** (or **1**) was separated from the aqueous phase and dried over anhydrous Na_2SO_4 (12 h). The filtered organic solutions were finally evaporated to dryness overnight, at a vacuum pressure of 0.1 mbar.

SANS experiments were performed at the KWS1 of the FRJ-2 research reactor at the Forschungszentrum Jülich.[14] Scattering data were obtained from $CDCl_3$ solutions of **1(D_2O)** at a concentration of 3.20×10^{-3} g cm^{-3}, and of **1** at 3.16×10^{-3} g cm^{-3}, respectively. The data were analysed in a standard procedure by applying corrections for background scattering and detector sensitivity, followed by a normalization which leads to the absolute value of the scattered intensity with a secondary standard. The scattered intensity is obtained as differential macroscopic cross-section $d\Sigma/d\Omega(Q)$ in cm^{-1} as a function of the momentum transfer $Q = (4\pi/\lambda)\sin(\theta/2)$ determined by the neutron wavelength λ and the scattering angle θ.

For data analysis, the complex structure of compound **1** depicted in Fig. 1 was simplified to a core–shell model, consisting of a central core and two concentric shells (compare Fig. 2). Each shell has a constant chemical composition, as expressed by the coherent scattering length density according to $\rho = \Sigma\, m_i b_i / V$ (m_i, number of atoms i in the shell). The core radius $r_c = 0.71$ nm refers to a spherical volume element which is occupied by 50 H_2O molecules (assuming a specific density

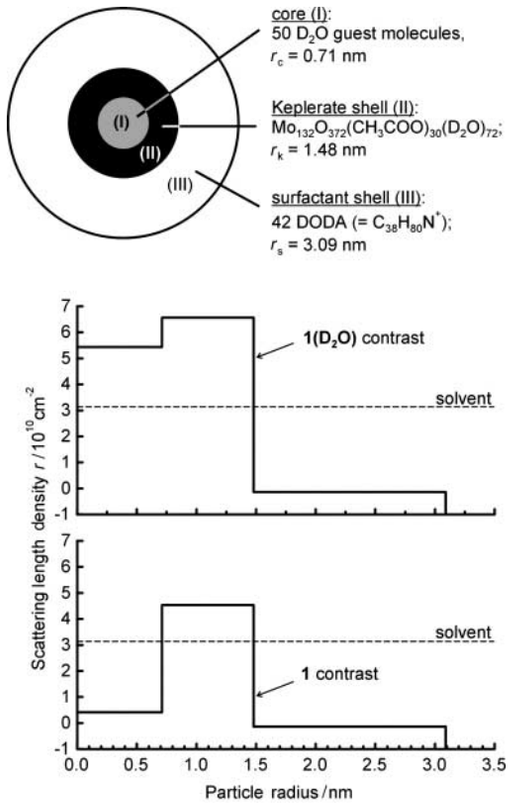

Fig. 2 Top: simplified core–shell model of **1(D$_2$O)**. The radius r_c of the central D_2O-filled cavity was calculated based on the bulk density of water, $d = 1.0$ g cm^{-3} (≈33.5 H_2O nm^{-3}); the outer radius r_k of the Keplerate shell was estimated from X-ray crystallographic data. The outer radius r_s of the surfactant shell was refined, based on SANS data of $CDCl_3$ solutions of **1(D$_2$O)** and **1**, respectively. Bottom: coherent scattering length densities from Table 1 with $r_s = 3.09$ nm.

of 1 g cm^{-3} (≈ 33.5 H_2O molecules nm^{-3})). Note that the calculated value for the core radius of our model here is similar but *not* identical with the average radius (0.85 nm) for the (non-spherical) nanocavity of **1**, as determined from X-ray crystallographic data.[12,13] The coherent scattering lengths b_i are tabulated,[15] so that the coherent scattering length density of each individual shell could be determined or at least given as a function of the corresponding volume V and its chemical structure. These values are shown in Table 1.

The scattering law for a core–shell model as depicted in Fig. 2 takes the form (1).[16] It is determined by the sum of

$$\frac{d\Sigma}{d\Omega}(Q) = n\left|\sum_{j=1}^{3}\Delta\rho_j V_j A_j(Q)\right|^2 \qquad (1)$$

the scattering amplitudes A times the volume V of a single shell with an inner and outer radius r_1 and r_2 according to eqn. (2)

$$V_j A_j(Q) = 4\pi\int_{x_1}^{x_2} dx.x^2 \sin x/x = 4\pi[g_j(x_2) - g_j(x_1)]/Q^3 \quad (2)$$

and $g_j = g(x_j) = \sin x_j - x_j \cos x_j$ ($x = Qr$). The scattering amplitude is normalized according to $A_j(Q = 0) = 1$. The interactions of neutrons and the sample is described by the difference between the coherent scattering length densities of the jth shell and the solvent $\Delta\rho_j = \rho_j - \rho_{CDCl_3}$ (see Table 1 and Fig. 2). The parameter n represents the SEC particle density which is an approximation for dilute solutions, where neutron scattering from individual particles occurs independently. The final form of the scattering law used for the fitting procedure is as in eqn. (3) with the scattering cross-section at $Q = 0$ according to eqn. (4). The scattering contrast is described by the two parameters $K_k = (\rho_k - \rho_{CDCl_3})/(\rho_c - \rho_k)$ and $K_s = (\rho_s - \rho_{CDCl_3})/(\rho_c - \rho_k)$. The unknown parameters of this core–shell model

Table 1 Coherent scattering length densities of the SEC shells containing H_2O and D_2O. The parameters K are defined in the text

Parameter	**1**	**1(D$_2$O)**
$\rho_c/10^{10}$ cm^{-2}	0.408	5.43
$\rho_k/10^{10}$ cm^{-2}	4.53	6.56
$\rho_s/10^{10}$ cm^{-2}; r/nm	$-3.73/(r_s^3 - r_k^3)$; 1.48	
$\rho_{CDCl_3}/10^{10}$ cm^{-2}	3.14	
K_k	−0.337	−3.03
K_s	$-0.243\rho_s + 0.762$	$-0.885\rho_s + 2.78$

$$\frac{d\Sigma}{d\Omega}(Q) = \frac{d\Sigma}{d\Omega}(Q=0)\left|\frac{3[g(x_c) + K_k g(x_k) + K_s(g(x_s) - g(x_k))]}{Q^3[r_c^3 + K_k r_k^3 + K_s(r_s^3 - r_k^3)]}\right|^2 \qquad (3)$$

$$\frac{d\Sigma}{d\Omega}(Q=0) = n\left|\frac{4\pi}{3}(\rho_c - \rho_k)[r_c^3 + K_k r_k^3 + K_s(r_s^3 - r_k^3)]\right|^2 \qquad (4)$$

are the outer particle radius r_s and the scattering at $Q = 0$ which were determined from the least-squares fitting routine.

^{1}H NMR spectroscopy

Spectra were recorded at the Institut für Angewandte Chemie, Berlin-Adlershof with a Varian Unity plus 300 spectrometer. Data for **1** [$CDCl_3$]: δ 0.88 (t, 6 H, $J = 6.75$ Hz, CH_3); 1.26 (m, 60 H, CH_2); 1.70 (m, 4 H, CH_2); 1.83 (s, CH_3CO_2); 3.30 (m, 6 H, CH_3N) and 3.55 (m, 4 H, NCH_2).

IR spectroscopy

IR spectra of compound **1** were recorded with a Bruker Equinox 55/S IR spectrometer. The transmission spectra were obtained from KBr pellets. Spectra of LB films were recorded with p-polarized radiation in reflection (gold wafer, angle of incidence 84°). The spectra of the Langmuir film were recorded with s-polarized radiation (angle of incidence 40°). A Riegler & Kirstein (R&K, Wiesbaden, Germany) film balance was used for these measurements. While recording the spectra, compression was stopped.

X-Ray reflectance

The experiments at the air–water interface were performed at Deutsches Synchrotron (DESY), Hamburg (HASYLAB, beam line BW 1).[17] The synchrotron beam was made monochromatic by Bragg reflection by a beryllium (002) crystal. The wavelength of the radiation was ≈1.36 Å. XRR experiments on films deposited on to solid supports were performed with a θ–2θ instrument (Stoe&Cie GmbH, Darmstadt, Germany) with Cu-Kα radiation ($\lambda = 1.54$ Å). The data were analysed using standard electrodynamic theory.[18] Literature values were taken for the electron density of the alkyl layers.[19] The electron density of the Keplerate cluster was derived from the X-ray crystallographic data.[13]

Ellipsometry

The measurements were performed with a Multiskop (Optrel GbR, Germany; 2 mW HeNe laser, $\lambda = 632.8$ nm) ellipsometer using null ellipsometry. The data were analysed with a fit program (Optrel GbR version 1.39) using standard Fresnel theory. The angles of incidence were 70° for solid substrates and 56° for measurement at the air–water interface. An R&K film balance was used for these measurements.

Complex refractive index

The real part of the index of refraction at 633 nm was determined by optical ellipsometry of thick LB layers on silicon to

be 1.54 ± 0.01. The film thickness of these samples was independently confirmed by X-ray reflectance. The imaginary part of the refractive index, k, was obtained from transmission UV-vis spectra to be 0.019 ± 0.001 using the relation $k = \varepsilon\rho\lambda/5.5\ M_r$, where λ is the wavelength and ε the molar absorptivity ($\varepsilon_{633\ nm} = 52 \times 10^3$ cm^2 mmol^{-1}). A molecular weight, M_r, of 44.75 kg mol^{-1} was used and the density, ρ, was determined to be 1.37 g cm^{-3}.

Surface coverage

The surface coverage of LB multilayers on quartz substrates was determined from transmission UV-vis spectra using the relation $\Gamma = N_A A_\lambda (\varepsilon_\lambda l)^{-1}$ where N_A is Avogadro's number, A_λ the experimentally determined absorbance, ε_λ the effective absorption coefficient [cm^2 mol^{-1}], and l the total number of LB layers counting both sides of the substrate ($\varepsilon_{470\ nm}$ 3.4×10^5 cm^2 mmol^{-1}).

Results and discussion

Investigations on the structure of discrete SECs

^{1}H NMR spectroscopy. The presence of surfactants in the SEC is confirmed by ^{1}H NMR spectroscopy. The resonance signals of the N-methyl protons are considerably broadened and high field shifted by 0.2 ppm as compared to the resonance frequencies of [DODA]Br in $CDCl_3$. The signal broadening may be rationalized in terms of a strong association of the surfactant and the Keplerate cluster, which would reduce the mobility of the dimethylammonium group. The shift of the resonance signal is ascribed to the chemically different local environment. We, therefore, conclude that the DODA surfactant points with its cationic headgroup to the negatively charged cluster surface. This SEC structure model is consistent with the solubility of the SEC in common organic solvents, such as chloroform or toluene.

IR spectroscopy. The transmission infrared spectrum of the SEC (KBr pellet) indicates that the alkyl chains are completely disordered.[20] The IR absorption bands of the symmetric and asymmetric CH_2-stretching modes occur at 2924 and 2852 cm^{-1}. The disorder of the alkyl chains is attributed to the strong curvature of the cluster core, which prevents the surfactants from arranging in a highly oriented co-aligned fashion (compare for instance the lamellar arrangement of DODA surfactants in the solid state structure of [DODA]Br[21]). The IR spectrum also shows the characteristic modes of the Keplerate cluster anion.

Analytical ultracentrifugation. The molecular weight of the SEC was confirmed by analytical ultracentrifugation (AUC).[22] Sedimentation velocity experiments give a sedimentation coefficient of $s = 10.21$ s. The hydrodynamic diameter, calculated from the sedimentation coefficient, is 4.73 nm and the molecular weight amounts to 45 kDa. Based on the accuracy of elemental analysis, we estimate the SEC composition as $(DODA)_{40 \pm x}(NH_4)_{2 \pm x}[(H_2O)_{50} \subset Mo_{132}O_{372}(CH_3CO_2)_{30}(H_2O)_{72}]$, with the molecular weight ranging from 43.7 (38 DODA cations) to 45.8 kDa (42 DODA cations). The experimentally determined molecular weight lies within these values, and we conclude that the hydrodynamic properties are consistent with the suggested model of discrete SECs. In less polar solvents, *e.g.* cyclohexane, we observed higher molecular weights (55.7 kDa), which may refer to a possible aggregation of SECs.

Small angle neutron scattering. An important aspect of neutron scattering techniques is the possibility to vary the contrast by using samples with different isotopes, since the interactions of neutrons with different isotopes of the same element are normally quite different. In our SANS experiment we use the different coherent scattering length densities of H_2O and D_2O as a means of contrast variation. (The corresponding scattering length densities are given in Table 1 and are depicted in Fig. 2 *versus* the particle size.)

The neutron scattering experiments were performed in a momentum transfer regime Q in which the atomistic resolution of the dynamic structure of **1** (Fig. 1c) is averaged out, so that we could interpret the SANS scattering data with a simplified core–shell model of the SEC, where the core (corresponding to the H_2O-filled nanocavity), the Keplerate shell (including the co-ordinated H_2O and acetate), and the surfactant shell are treated as separate spherical entities (Fig. 2). Subdividing the POM into a core and a Keplerate shell enables us to distinguish between H_2O guest molecules that are hosted in the nanocavity, and H_2O ligands that are coordinated to the Keplerate shell. The most uncertain parameter of our SEC model is the diffuse boundary between the surfactant shell and the solvent, because under ambient conditions the alkyl chains are dynamically distorted. Furthermore, solvent molecules penetrate into the surfactant shell, which leads to a smeared contrast differentiation in the SANS experiments. Since we presently lack a valid model of the SEC–solvent interface, we treat the outer radius r_s of the SEC as an independent variable and refine it according to eqns. (3) and (4).

Scattering data were collected from $CDCl_3$ solutions of compound **1** as well as from D_2O-exchanged SECs, **1(D$_2$O)** (see Experimental section for details). For the composition of **1(D$_2$O)** we constructed three different models: Model A corresponds to the molecular formula $(DODA)_{42}[(D_2O)_{50} \subset Mo_{132}O_{372}(CH_3CO_2)_{30}(D_2O)_{72}]$ (assuming exchange of *all* H_2O molecules), Model B to $(DODA)_{42}[(D_2O)_{50} \subset Mo_{132}O_{372}(CH_3CO_2)_{30}(H_2O)_{72}]$ (assuming complete exchange of *non-co-ordinated* H_2O molecules), and Model C to the molecular formula of **1** (assuming that D_2O exchange did not occur). Finally, we used the refinement parameter r_s as a sensitive quality factor for the validation of the different models A–C. The idea behind this is that the SANS data refinement for **1** as well as **1(D$_2$O)** should independently lead to the same r_s value for both data sets, considering the fact that the structure and composition of the surfactant shell should be identical for both samples.

The experimental results are shown in Fig. 3. The scattering from the two samples shows slightly different intensities. The fit of the data with eqn. (3) using two parameters, namely the outer radius r_s and the scattering at $Q = 0$, is represented in Fig. 3 by the two solid lines, which describe the data well. The outer radius of **1** is determined to be $r_s = 3.09 \pm 0.026$ nm as depicted in the inset of Fig. 3. The r_s value of **1** is compared with those r_s from **1(D$_2$O)** that were refined with three different contrasts, corresponding to model A, B, or C. Fig. 3 (inset) shows that the best agreement is obtained for model A, thus proposing a complete exchange of H_2O against D_2O in the core and the Keplerate shell. This finding seems reasonable, if we hypothesize that the predominant reaction path for H_2O/D_2O exchange will be the rapid exchange of acidic protons against deuterons. Other reaction pathways (*e.g.* the slow diffusion of H_2O (D_2O, respectively) through the (Mo–O) 9-ring openings of the Keplerate) probably will make a minor contribution to the exchange process.

Investigations on Langmuir monolayers of compound 1

Langmuir isotherms. The SEC spreads at the air–water interface and the π–A isotherms are reproducible. A representative example of such an isotherm recorded at 18 °C on a pure water subphase after 30 minutes of equilibration is shown in Fig. 4. There are no distinct phase transitions in the isotherm at this temperature. The collapse occurs at approximately 60 mN m^{-1} and indicates a stable film. There is no significant change in film

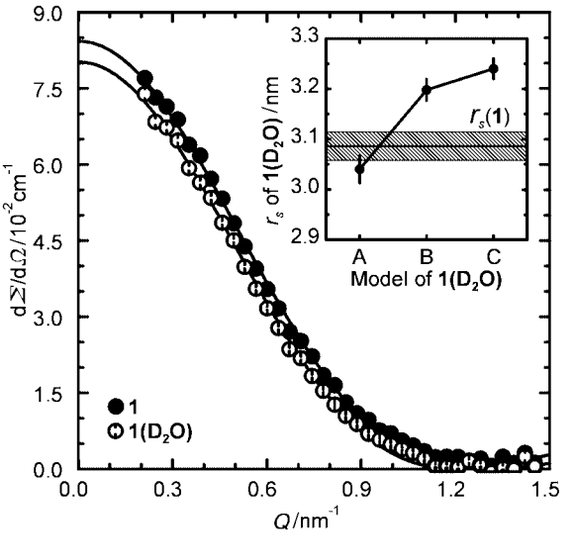

Fig. 3 Experimental and fitted SANS curves for dilute $CDCl_3$ solutions of compounds **1** and **1(D$_2$O)**, respectively. The inset shows refined values for the outer radius r_s in **1(D$_2$O)** assuming different models (A–C) for the D_2O content of **1(D$_2$O)**. The r_s values for both samples were identical within the experimental error only for Model A, which corresponds to the molecular formula $(DODA)_{42}$-$[(D_2O)_{50} \subset Mo_{132}O_{372}(CH_3CO_2)_{30}(D_2O)_{72}]$ (assuming a complete exchange of H_2O molecules).

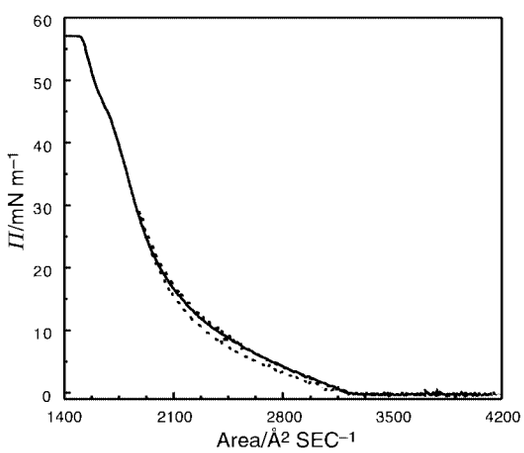

Fig. 4 Representative example of the surface pressure *vs.* area (π–A) isotherm of compound **1**, measured at 18 °C on a pure water subphase (recorded after 30 min of equilibration). The solid line shows the compression and the dotted line a compression–expansion cycle (maximum pressure 30 mN m^{-1}). The collapse pressure is approximately 58 mN m^{-1} with an area of 15 nm^2 per SEC, which corresponds to a sphere with diameter 4.4 nm.

area if the monolayer is held at constant pressure (30 mN m^{-1}) for a period of 12 hours, which indicates a high stability of the monolayer. The area at the collapse pressure is 15 nm^2 per SEC, which corresponds to a sphere with diameter 4.4 nm, in good agreement with the proposed structure of the SEC.[23] An alternative bilayer model consisting of a separate surfactant monolayer in contact with a diffuse layer of hydrated cluster anions in the aqueous subphase can be ruled out: in this case, the area at the collapse of 15 nm^2 would correspond to 40 surfactant molecules, or 0.38 nm^2 per DODA, which is far too small for DODA.[24]

Upon expansion a slight hysteresis is observed. A second compression–expansion cycle gives identical results. The isotherm also shows a shoulder at 17 nm^2 per SEC, which becomes more pronounced at elevated temperature and disappears at lower temperature. This behavior may be attributed to a phase transition of the surfactants in this temperature range, which was similarly observed in DSC measurements.[25]

BAM. The uniformity of the monolayer was investigated by Brewster angle microscopy. Fig. 5 shows the BAM images of a SEC monolayer recorded at different pressures. The gas phase region at low pressure consists of domains of uncharacteristic shape and size. Upon decreasing the surface area the domains start to fuse (0 mN m^{-1}). At a surface pressure of 5 mN m^{-1} the film is almost uniform and stays like this upon further compression. Upon expansion the inverse behavior is observed: the Langmuir film remains uniform up to 0 mN m^{-1}, after which it segregates into domains.

Ellipsometry. Optical ellipsometry was used to determine the thickness of the Langmuir monolayers of compound **1**. The surface pressure π and the ellipsometric parameters, Δ and Ψ, were recorded simultaneously. Owing to the small changes of film thickness, the parameter Ψ remains constant during compression. Fig. 6 summarizes the data.

First, we note that the decline of Δ upon reducing the surface area is characteristic for a Langmuir layer with a refractive index larger than 1.33. It is not possible to determine the refractive index and the film thickness simultaneously from these data because there is only a change in one of the two ellipsometric parameters.[26] As an approximation, the refractive index determined from thick films of compound **1** can be used to compute the film thickness ($1.54 - 0.019i$). In this case, the apparent or effective film thickness at the collapse pressure is 1.8 nm. This value is smaller than the experimental diameter of a SEC as determined from Langmuir isotherm (4.4 nm) or TEM (4.5 nm) investigations.[12] If one takes into account that the occupied volume fraction in a single layer of close packed spheres is only 60%, the actual film thickness amounts to 3 nm. This value is still smaller than the diameter of **1** because the chosen refractive index represents an approximation. The effective film refractive index will, in fact, be smaller if we consider the hypothesis that the SECs immerse in the water surface (see Fig. 7b). The immersion depth of a small sphere in the water interface is given by $d/2\,[1 - \cos(180 - \theta)]$, where d is the diameter of the sphere and θ is the advancing water contact angle.[27] The water contact angle, determined from multilayer LB films on silicon substrates, is 97°. The immersion depth is, therefore, predicted to be 0.44 d. The composition of the interface then is 60% SEC, 18% water and 22% air. The effective refractive index of the Langmuir film then amounts to $N_{eff} = 1.380 - 0.011i$.[28] Under these assumptions, the film thickness is approximately 6 nm, which is slightly too large. Although the ellipsometric data cannot unambiguously ascertain the foregoing hypothesis because the film is too thin, the analysis suggests that the SEC–water interface is not sharply defined. The discussion implies, however, that the computed values for the film thickness are in agreement with a single SEC monolayer existing at the air–water interface, while multilayers can be ruled out.

X-Ray reflectance. A more detailed view of the Langmuir monolayer structure is revealed by XRR because it provides the electron density profile along the interface normal. The experimental and computed reflectance data, as well as the corresponding electron density profile of the monolayer at 30 mN m^{-1}, are shown in Fig. 7(a). The best fit of the experimental data was achieved with a three-box model, shown in Fig. 7(b), using the following parameters: water ($\rho_{el} = 0.33$ Å^{-3}), box a ($\rho_{el} = 0.37$ Å^{-3}; $d = 1.3$ nm; $\tau = 0.5$ nm), box b ($\rho_{el} = 0.085$ Å^{-3}; $d = 0.8$ nm; $\tau = 0.5$ nm), box c ($\rho_{el} = 0.37$ Å^{-3}; $d = 0.4$ nm; $\tau = 0.4$ nm), air ($\rho_{el} = 0$). Here ρ_{el} is the electron density, d the thickness of the box, and τ the interfacial roughness. The asymmetric structure of the interface is reflected in different thickness values d. The total film thickness is 2.5 nm at this surface pressure.

The mathematical description of the interface is based on a stack of semi-infinite boxes, each with a uniform electron

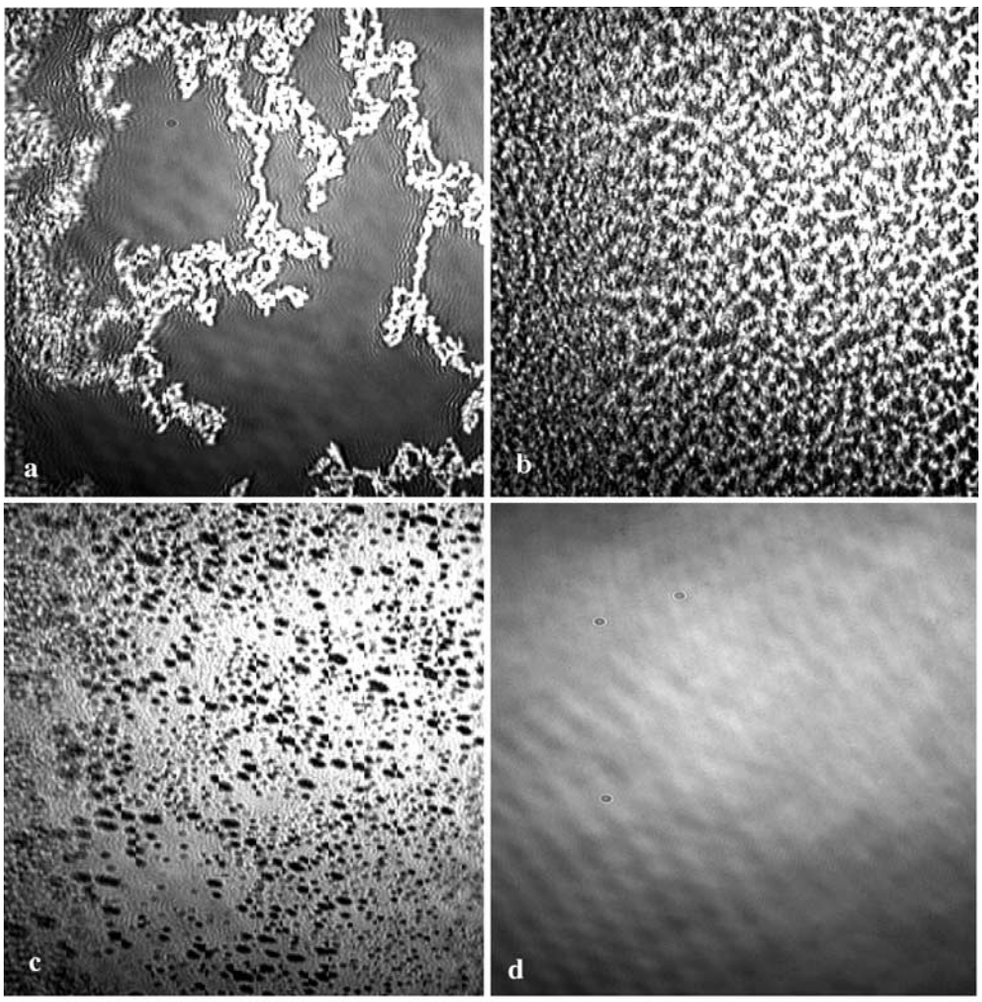

Fig. 5 BAM images of the Langmuir monolayer of compound **1** (15 °C, pure water, image area 500 × 500 μm). Images a–c were recorded at zero surface pressure at 34 (a), 31 (b), and 29 nm² per SEC (c), respectively. Image d was recorded at a surface pressure of 5 mN m^{-1}. After the spreading of **1**, film domains of uncharacteristic shape and size appear, which begin to fuse upon compression. At a surface pressure of 5 mN m^{-1} the monolayer becomes homogeneous. (Compression direction from bottom to top of the image.)

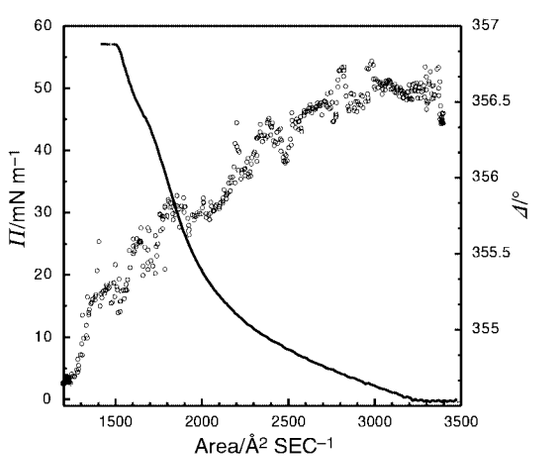

Fig. 6 Surface area and ellipsometric parameter Δ of a monolayer of compound **1** at the air–water interface as a function of surface pressure π (see text for details).

density and thickness; to account for a smooth transition from one box to the next a surface roughness is introduced at each interface. In the case of the Langmuir monolayer of compound **1** this is an approximation because of the spherical structure of the SEC. Therefore, the electron density, that is the composition, is *not* uniform in the plane of the monolayer. The absolute values for the box parameters should, therefore, be regarded as qualitative indicators. However, the three-box model supports the presence of a monolayer of SECs at the air–water interface and is consistent with the ellipsometric data.

IR spectroscopy. Information about the conformation of the surfactant alkyl chains in the monolayer is obtained by reflection IR spectroscopy of the Langmuir monolayer of compound **1** as a function of surface pressure. At low pressure (π < 5 mN m^{-1}, area < 32 nm² per SEC) the asymmetric CH_2 stretching mode is observed at 2924 cm^{-1}, indicating many *gauche* defects in the alkyl chains. Upon compression of the monolayer the band is continuously shifted to a final value of 2919 cm^{-1} close to the collapse pressure. Similarly, the symmetric CH_2 stretching mode shifts from 2854 (expanded) to 2850 cm^{-1} (compressed state). In the compressed state the alkyl chains are predominantly in an all-*trans* configuration. However, the alkyl chains are not crystalline at this stage as a comparison with solid [DODA]Br shows (2916 and 2848 cm^{-1}). From the ratio of absorption intensities from the symmetric and asymmetric CH_2 stretching modes information about the orientation can be deduced because the infrared spectrum is recorded with polarized radiation. In the transmission IR spectrum of [DODA]Br dispersed in KBr (isotropic) the ratio is 1.35:1 and in the Langmuir monolayer it is 1.36 ± 0.01:1 (π = 67 mN m^{-1}). The similarity of the values suggests that the methylene groups in the SEC Langmuir monolayer are not oriented. A uniform distribution of the CH_2 orientations is expected for a core–shell structure, in which the surfactants are evenly distributed over the surface of the spherical core.

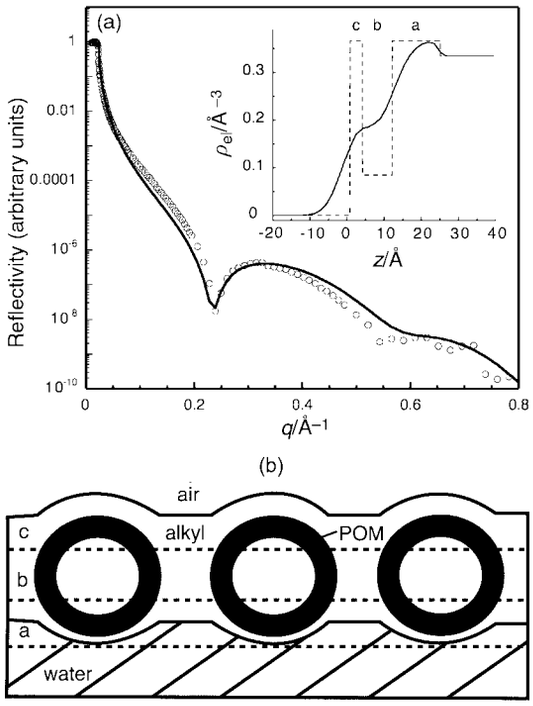

Fig. 7 (a) The experimental (open circles) and calculated (solid line) X-ray reflectance curves for a monolayer of compound **1** at the air–water interface ($\lambda = 1.36$ Å, $\pi = 30$ mN m^{-1}). The inset shows the calculated electron density profile (solid line) and the corresponding box model (dotted line) normal to the interface. The data confirm the presence of a monolayer of surfactant-encapsulated clusters, **1**, at the air–water interface. (b) Simplified scheme of the SEC at the air–water interface (not to scale) and the mathematical model used for the fit of XRR data. The interface is approximated by a stack of plane-parallel, homogeneous semi-infinite boxes, each characterized by a uniform film thickness and electron density (depicted as dashed lines in Figs. 7(a) and 8). To ensure a smooth transition between each box a surface roughness is introduced at each interface (depicted as the solid line in Figs. 7(a) and 8). Box a is associated with the SEC–water interface, b contains the Keplerate clusters as well as interstitial surfactants, and c represents the SEC–air interface. The asymmetric structure of the monolayer is reflected in different thickness values for each box. The variation of the electron density in the horizontal direction is not taken into account in the current model.

Langmuir–Blodgett films

Langmuir–Blodgett film transfer. The Langmuir monolayers can be transferred on to solid substrates such as silicon or quartz. The transfer ratio is close to unity for all transfer pressures investigated. In the following a representative example will be discussed, where the Langmuir monolayer was transferred at a pressure of 20 mN m^{-1}. UV-vis spectroscopy of LB films on quartz substrates confirms a linear growth of the LB multilayer (not shown). The surface coverage is 2.5×10^{12} SECs cm^{-2} or 40 nm^2 per SEC. This value is considerably larger than the area of a single SEC (approx. 15 nm^2 at the collapse pressure), because the film was transferred at a low pressure. The determination of the thickness by ellipsometry also confirms linear growth of the multilayer (not shown). The average thickness per layer is 2.1 nm, which is smaller than the diameter of the SEC (4.4 nm) and can be rationalized if the low transfer pressure is taken into account. The surface coverage of approximately 50% is in agreement with results from UV-vis transmission measurements. The ellipsometric parameters, Δ and Ψ, are constant if the sample is rotated in the direction of the surface normal. This demonstrates that the multilayer is isotropic in the plane of the film. In summary, the data indicate that transfer at 20 mN m^{-1} results in LB films with a surface coverage of approximately 50%.

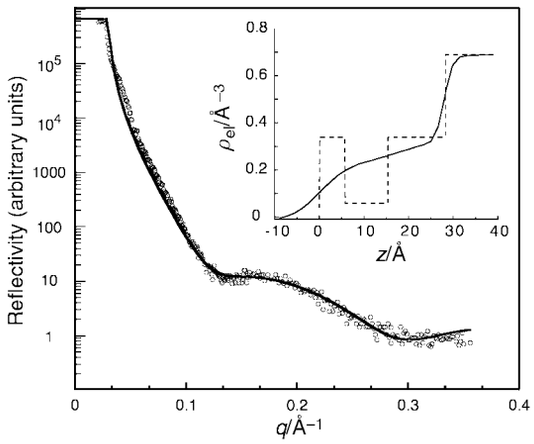

Fig. 8 Experimental (open circles) and calculated (solid line) X-ray reflectance ($\lambda = 1.54$ Å) of a monolayer of compound **1** transferred to a silicon substrate. The solid line shows the best data fit based on the three-box model (see Fig. 7b). This model is consistent with a monolayer of **1** consisting of surfactant-encapsulated Keplerate clusters (see text for details).

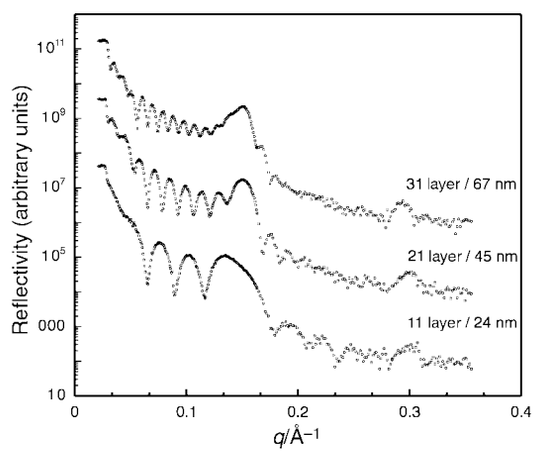

Fig. 9 X-Ray reflectance curves for a LB film of compound **1** consisting of 11, 21, and 31 SEC transfer cycles (transferred at a surface pressure $\pi = 20$ mN m^{-1}). The Kiessig interference fringes indicate a uniform film thickness, which increases by a constant increment. The thickness of a transferred SEC monolayer is 2.1 nm and the translation period 4.2 nm, respectively. Bragg reflections occur at $q = 0.15$ and 0.3 indicating an intrinsic tendency of SEC aggregates to adopt a 3-dimensional, highly ordered solid state architecture. (XRR curves are shifted in the y direction for clarity.)

X-Ray reflectance. The internal structure of the LB films was investigated by X-ray reflectance. Fig. 8 shows the XRR data as well as the calculated reflectance curves for a single LB layer of compound **1** deposited on to a silicon wafer. The three-box model employed previously (compare Fig. 7b) provides an excellent fit (solid line) of the experimental data (silicon ($\rho_{el} = 0.69$ Å^{-3}), box a ($\rho_{el} = 0.34$ Å^{-3}; $d = 1.3$ nm; $\tau = 0.8$ nm), box b ($\rho_{el} = 0.06$ Å^{-3}; $d = 0.9$ nm; $\tau = 1.1$ nm), box c ($\rho_{el} = 0.34$ Å^{-3}; $d = 0.6$ nm; $\tau = 0.6$ nm), air ($\rho_{el} = 0$)).

Within the limits of the chosen monolayer model and the experimental accuracy of reflectance data, the analysis confirms the core–shell structure of compound **1** in the transferred monolayer. The surface roughness is 0.8 nm for the silicon–SEC interface and 0.6 nm for the air–SEC interface, respectively. The total film thickness is 2.8 nm, in agreement with the previous results.

The reflectance curves for LB films with 11, 21, and 31 transfer cycles (tc) are shown in Fig. 9. The Kiessig interference fringes indicate that the LB layers have a uniform thickness. The average thickness per layer amounts to 2.1 nm and is in excellent agreement with the previous results. In addition, two

Bragg reflections are seen at $q = 0.15$ and 0.3. The amplitude modulation of the Kiessig fringes to the left and right side of the Bragg peak, as well as the unusual shape of the Bragg peak, results from interference effects; the film is no longer periodic because it consists of an odd number of layers.[29] Applying the Bragg equation ($m\lambda = 2d \sin \theta$, where m is the order, d the translation period, and θ the reflection angle) the translation period is 4.2 nm. This value is in excellent agreement with the previously reported size of the SEC determined by TEM.[12] We note that there are only half as many Kiessig fringes before the first Bragg peak than there are transferred Langmuir monolayers. This implies that the translation period includes two Langmuir monolayers. We, therefore, conclude that two transfer cycles (up- and down-stroke) are required to form one densely packed layer. The reason for this can be rationalized in terms of the low transfer pressure, which results in a surface coverage of approximately 50% per transfer. It is remarkable that this kind of LB deposition results in a highly ordered architecture. The structural flexibility that is required for this adaptability is most likely provided by the mobile surfactant matrix. The structural reorganization that takes place during deposition is reminiscent of a self-annealing process found in self-organizing systems.

IR spectroscopy. Analysis of reflection-absorption infrared spectra of SEC multilayers on gold substrates reveals that the disorder, that is the number of *gauche* defects, of the alkyl chains increases upon transfer. The CH_2 stretching modes occur at 2923 and 2851 cm^{-1}, which is similar to the positions in the transmission spectrum of the SEC dispersed in a KBr pellet (2924 and 2852 cm^{-1}). The positions of the CH_2-stretching modes in LB films are independent of the transfer pressure in the range 20–40 mN m^{-1}. The transfer-induced loss of order in the alkyl moieties can be understood if the surfactant shell is considered as a mobile matrix, which reorganizes into a compact film upon transfer. Disordered alkyl chains are also confirmed by the advancing water contact angle of 97°. For comparison, a highly ordered, methyl terminated surface has a contact angle of 110–115°.[30] The hydrophobic nature of the LB interface demonstrates how efficiently the surfactants shield the internal, hydrophilic POM core.

Conclusions and outlook

The intriguing supramolecular architecture of SECs such as compound **1**, as well as their potentially interesting functional properties, might well be compared to the structures of naturally occurring capsule-forming proteins such as the iron storage protein ferritin,[31] or the capsid proteins from certain classes of viruses (Fig. 10). Mineral deposition in the iron storage protein (ferritin), for instance, may be regarded as an archetypal biological model for the formation of a nanocrystalline mineral phase within a confined space. Current biomimetic strategies to achieve similar properties include mineralization in block copolymer micelles,[32] or biotechnologically produced capsule-forming proteins.[33,34] We note that, although the nanocavity of **1** is at an order of magnitude smaller than the corresponding void volume of apoferritin or virus capsids, it is considerably larger than most of the hitherto described supramolecular organic[35] or inorganic[36] host systems. Efforts to characterize *functional* properties (*e.g.* host–guest chemistry, catalytic activity, electrochemistry) of (surfactant-encapsulated) Keplerates and related giant POM clusters,[37] therefore, seem highly rewarding.

The results obtained so far show that the gross structural features of compound **1** can successfully be investigated by SANS experiments, which add further support to our core–shell model of discrete surfactant-encapsulated clusters. This experiment is a first step towards studying the distribution of guest molecules (in the present case: H_2O) hosted in the

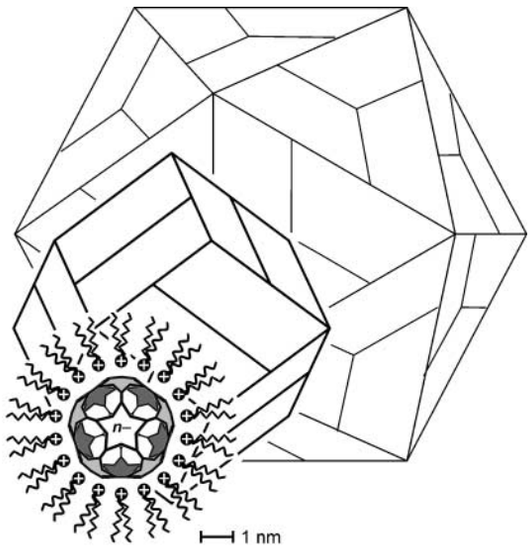

Fig. 10 Size and symmetry of compound **1** as compared with some naturally occurring self-assembling oligomeric peptides (schematically). The surfactant-encapsulated Keplerate cluster (in front) consists of 12 pentagonal $\{Mo/Mo_5\}$ subunits situated at the vertices of an icosahedron that are linked by a further 30 $\{Mo_2\}$ units. The cationic surfactants are evenly distributed over the negatively charged polyoxomolybdate cluster, with their charged head-groups pointing toward the cluster surface. The inner cavity of the Keplerate cluster has an average diameter of 1.7 nm, which contains *ca.* 50 H_2O molecules. The iron storage protein ferritin (middle) consists of an oligomeric protein shell and a core of poorly crystalline iron(III) hydroxide oxide. 12 subunit dimers form the faces of an imaginary rhombic dodecahedron. The apoferritin shell encloses a nearly spherical cavity of 8 nm diameter which is typically loaded with some 1000–3000 iron(III) ions per core. In the back a typical arrangement of the subunits of a virus coat protein (*e.g.* comovirus) is shown. Typical values for the outer diameter of the icosahedral virus particles range from 17 to 45 nm.

Keplerate nanocavity. In future investigations the contrast factor K_s could be matched to zero by applying the appropriate mixture of solvents, in order to characterize the molecular composition of the encapsulated clusters with higher sensitivity. Then, scattering would occur only from the core and the Keplerate shell, while the surfactant shell would be "invisible". Information from SANS studies will be complemented by NMR studies on the dynamic exchange properties of SECs.

In terms of technical applications (*e.g.* heterogeneous catalysis, sensing applications, protective coatings) it will be important to address the question of how to arrange POMs into 3-dimensional supramolecular architectures in a controlled and predictable manner. Our contributions to this topic currently include thin films of SECs, as presented here, and self-assembling layer-by-layer films of POMs and polyelectrolytes, which are presented elsewhere (Fig. 11).[38]

Considerable efforts were made to analyse the structure of Langmuir and Langmuir–Blodgett films of compound **1**. The SEC spreads at the air–water interface to form stable, reproducible Langmuir monolayers. Using X-ray reflectance, we were able to show that the core–shell architecture of discrete SECs is preserved at the air–water interface. IR reflection spectroscopy of the Langmuir monolayers indicates that the CH_2 groups of the surfactant alkyl chains are conformationally disordered at low surface pressures, and that the number of *gauche* defects decreases upon compression. Within the experimental accuracy of the employed methods, there is no sign of dissociation or of an extensive structural reorganization of the surfactant-encapsulated Keplerate cluster at the air–water interface.[39] This result seems surprising to us, since a direct contact between the hydrophobic surfactant shell and the aqueous solution should

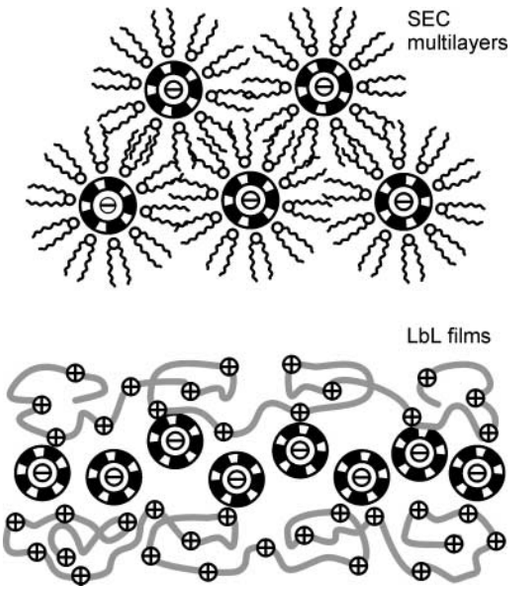

Fig. 11 Schematic representation of POM–surfactant composites of current investigations. Top: highly ordered multilayers of surfactant-encapsulated polyoxometalate clusters. Bottom: layer-by-layer (LbL) films of polyoxometalates and charged macromolecules (not to scale).

be unfavorable in terms of surface energies, and one may expect the SECs to form compact droplets on the water surface rather than to spread as a monolayer.[40] Apparently, there must be other factors (that we are currently unable to describe) which may help to stabilize the SEC monolayer at the air–water interface.[41]

Langmuir–Blodgett (LB) transfer of compressed monolayers on to a solid substrate leads to homogeneous multilayers of compound **1**. In the XRR spectra of LB multilayers of **1** multiple Bragg reflections appear, thus indicating an intrinsic tendency of SECs to adapt a 3-dimensional, highly ordered solid state structure. Analysis of the X-ray reflectance data proves in a quantitative way that the core–shell structure of the SEC is preserved upon LB transfer. The alkyl chains are completely disordered in the LB film.

Model studies using structurally uniform, monodisperse SECs such as compound **1** may help to improve the design of technologically equally interesting composite materials of surfactants and inorganic compounds (*e.g.* quantum-confined SECs of semiconductors[42] or precious metals) that will be suitable for LB film transfer. Owing to the weak hydrophobic interactions between neighboring SECs, the surfactant shell provides a mobile matrix thus allowing the encapsulated POM clusters to rearrange their relative positions. Consequently, SEC-based thin films and materials possess the intrinsic property of self-annealing and of self-repairing structural packing defects under mild and non-destructive ("biological") conditions.

Acknowledgements

The authors wish to thank Helmuth Möhwald for valuable discussions, Gerald Brezesinski for conducting the synchrotron X-ray reflectance measurements at the air–water interface, Arne Gericke for the infrared measurements of Langmuir monolayers, Randolf Teppner for assisting in the ellipsometric measurements, and Michael J. Koop for preparing the Keplerate starting material. This work was supported by the Max-Planck Society. D. V. thanks the Fonds der Chemischen Industrie (FCI) for a Liebig fellowship. Financial support by the Deutsche Forschungsgemeinschaft (DFG) and the Bundesministerium für Bildung und Forschung (BMBF) is gratefully acknowledged.

References

1 M. T. Pope and A. Müller, *Angew. Chem.*, *Int. Ed. Engl.*, 1991, **30**, 34; M. T. Pope and A. Müller, eds., *Polyoxometalates: From platonic solids to antiretroviral activity*, Kluwer, Dordrecht, 1994.
2 I. V. Kozhevnikov, *Chem. Rev.*, 1998, **98**, 171; N. Mizuno and M. Misono, *Chem. Rev.*, 1998, **98**, 199.
3 I. A. Weinstock, *Chem. Rev.*, 1998, **98**, 113; M. Sadakane and E. Steckhan, *Chem. Rev.*, 1998, **98**, 219.
4 T. Yamase, *Chem. Rev.*, 1998, **98**, 307.
5 J. T. Rhule, C. L. Hill, D. A. Judd and R. F. Schinazi, *Chem. Rev.*, 1998, **98**, 327.
6 D. E. Katsoulis, *Chem. Rev.*, 1998, **98**, 359.
7 J. H. Fendler, *Membrane mimetic approach to advanced materials*, Springer, Berlin, 1994, Advances in polymer science series, vol. 113.
8 Examples of technologically important compounds which exhibit strong size-dependent physical and chemical properties range from catalytically active, highly dispersed metal nanocolloids (*e.g.* Pt, Pd, Rh), quantum confined semiconductor nanoparticles (CdS, CdSe) to nanoscale ferrimagnetic particles (*e.g.* γ-Fe_2O_3) and nanocomposite magnetic alloys. See: J. H. Fendler, ed., *Nanoparticles and nanostructured films: preparation, characterization and applications*, Wiley-VCH, Weinheim, 1998.
9 M. Clemente-León, C. Mingotaud, B. Agricole, C. J. Gómez-García, E. Coronado and P. Delhaes, *Angew. Chem.*, *Int. Ed. Engl.*, 1997, **36**, 1114; C. G. Janauer, A. Dobley, J. D. Guo, P. Zavalij and M. S. Whittingham, *Chem. Mater.*, 1996, **8**, 2096; A. Stein, M. Fendorf, T. P. Jarvie, K. T. Müller, A. J. Benesi and T. E. Mallouk, *Chem. Mater.*, 1995, **7**, 304.
10 A. Müller, P. Kögerler and C. Kuhlmann, *Chem. Commun.*, 1999, **15**, 1347.
11 D. G. Kurth, P. Lehmann, D. Volkmer, H. Cölfen, M. J. Koop, A. Müller and A. Du Chesne, *Chem. Eur. J.*, 2000, **6**, 385; D. G. Kurth and D. Volkmer, in *Polyoxometalates: Self-assembled beautiful structures, adaptable properties, industrial applications*, eds. A. Müller and M. T. Pope, Kluwer, submitted.
12 D. Volkmer, A. Du Chesne, D. G. Kurth, H. Schnablegger, P. Lehmann, M. J. Koop and A. Müller, *J. Am. Chem. Soc.*, 2000, **122**, 1995.
13 A. Müller, E. Krickemeyer, H. Bögge, M. Schmidtmann and F. Peters, *Angew. Chem.*, *Int. Ed.*, 1998, **37**, 3360; A. Müller, V. P. Fedin, C. Kuhlmann, H. Bögge and M. Schmidtmann, *Chem. Commun.*, 1999, **10**, 927; A. Müller, S. Polarz, S. K. Das, E. Krickemeyer, H. Bögge, M. Schmidtmann and B. Hauptfleisch, *Angew. Chem.*, *Int. Ed.*, 1999, **38**, 3241.
14 *Neutronenstreuexperimente am FRJ-2 in Jülich*, Forschungszentrum Jülich, 1997.
15 *Neutron News*, 1992, **3**, 29.
16 J. S. Higgins and H. Benoit, *Polymers and Neutron Scattering*, Clarendon Press, Oxford, 1994.
17 K. Kjaer, J. Majewski, H. Schulte-Schrepping and J. Weigelt, *HASYLAB Annu. Rep.*, 1992, 589.
18 A. Asmussen and H. Riegler, *J. Chem. Phys.*, 1996, **104**, 8151.
19 T. P. Russell, *Mater. Sci. Rep.*, 1990, **5**, 171.
20 R. G. Snyder, S. L. Hsu and S. Krimm, *Spectrochim. Acta*, *Part A*, 1978, **34**, 395.
21 [DODA]Br (monohydrate), CSD entry code CIYWOW20. K. Okuyama, Y. Soboi, N. Iijima, K. Hirabayashi, T. Kunitake and T. Kajiyama, *Bull. Chem. Soc. Jpn.*, 1988, **61**, 1485.
22 Attempts to determine the molecular weight of the parent Keplerate cluster by AUC measurements were not successful. A possible explanation is that some of the cluster anions decompose or form aggregates during the measurement. The determination of the molecular weight is complicated if several species with different molecular weights are present in the solutions.
23 The surfactant shells of neighboring SECs in the film can penetrate each other, thus leading to an apparently smaller diameter as compared with a molecular model of an isolated discrete SEC.
24 The molecular area per [DODA]Br at film collapse (48 mN m^{-1}, 20 °C) was determined to be 0.54 nm^2 per molecule. On an aqueous subphase containing $[(H_2O)_n \subset Mo_{132}O_{372}(CH_3CO_2)_{30}(H_2O)_{72}]^{42-}$ at a concentration of 1 μmol L^{-1} the collapse area is similar (0.55 nm^2 per molecule).
25 Differential scanning calorimetry (DSC) shows an endothermic phase transition at 10–15 °C, attributed to alkyl chain melting, and an exothermic one at 40–45 °C, which has not been assigned yet. A more detailed analysis of the Langmuir monolayer phase behavior will be presented elsewhere.
26 R. M. A. Assam and N. M. Bashara, *Ellipsometry and Polarized Light*, Elsevier, Amsterdam, 1987.

27 Z. Hórvölgyi, Z. Medveczky and M. Zrinyi, *Colloid. Polym. Sci.*, 1993, **271**, 396. This analysis is solely based on surface energies. The contribution of gravitation force to the immersion depth can be neglected for very small spheres.
28 The effective refractive index of the film was calculated according to D. A. G. Bruggeman, *Ann. Phys.*, 1935, **24**, 636.
29 F. Rieutord, J. J. Benattar, L. Bosio, P. Robin, C. Blot and R. de Kouchkovsky, *J. Phys.* (*Paris*), 1987, **48**, 679.
30 C. D. Bain, E. B. Troughton, Y.-T. Tao, J. Evall, G. M. Whitesides and R. G. Nuzzo, *J. Am. Chem. Soc.*, 1989, **111**, 321.
31 P. M. Harrison and P. Arosio, *Biochim. Biophys. Acta – Bioenergetics*, 1996, **1275**, 161; D. Volkmer, *Biomineralization*, in *Encyclopedia of Separation Science*, Academic Press Ltd., New York, in the press.
32 M. Möller and J. P. Spatz, *Curr. Opin. Colloid Interface Sci.*, 1997, **2**, 177.
33 T. Douglas and M. Young, *Nature* (*London*), 1998, **393**, 152; S. Gider, D. D. Awschalom, T. Douglas, S. Mann and M. Chaparala, *Science*, 1995, **268**, 77.
34 "Classical" approaches that make use of the entrapped water content of oil/water microemulsions as a rule suffer from relatively broad size distributions of the precipitated nanoparticulate materials due to the non-uniform sizes of the droplets in the (reversed) microemulsions.
35 J. Rebek, *Acc. Chem. Res.*, 1999, **32**, 278.
36 The free diameters of the channels in different types of zeolites, based on the crystallographic atomic coordinates of the type materials and an oxygen radius of 1.35 Å, typically range from 0.25 to 0.8 nm. See: W. M. Meier, D. H. Olson and Ch. Baerlocher, *Atlas of Zeolite Structure Types*, 4th rev. edn., 1996, http://www.iza-sc.ethz.ch/IZA-SC/Atlas/Table2.html
37 A. Müller, F. Peters, M. T. Pope and D. Gatteschi, *Chem. Rev.*, 1998, **98**, 239.
38 F. Caruso, D. G. Kurth, D. Volkmer, M. J. Koop and A. Müller, *Langmuir*, 1998, **14**, 3462; D. G. Kurth, D. Volkmer, M. Ruttorf, B. Richter and A. Müller, *Chem. Mater.*, accepted for publication.
39 Structural reorganization has been proposed for dendrimers at the air–water interface. See for instance: P. M. Saville, P. A. Reynolds, L. W. White, C. J. Hawker, J. M. J Fréchet, K. L. Wooley, J. Penfold and J. R. P. Webster, *J. Phys. Chem.*, 1995, **99**, 8283; A. H. J. Schenning, C. Elissen-Roman, J.-W. Weener, M. W. P. L. Baars, S. J. van der Gaast and E. W. Meijer, *J. Am. Chem. Soc.*, 1998, **120**, 8199.
40 In general, hydrophobic compounds do not spread at the air–water interface but aggregate and float as droplets or lenses on the water surface. Amphiphilic compounds that spread at the air–water interface have polar or charged groups that interact with the water molecules. A. W. Adamson and A. P. Gast, *Physical chemistry of surfaces*, 6th edn., Wiley, New York, 1997.
41 The hydrophobic nature of the SECs is demonstrated by its high solubility in apolar organic solvents and its wetting behavior. There are only few literature examples of hydrophobic molecules that form stable and reproducible Langmuir monolayers. See for instance: T. Pfohl, H. Möhwald and H. Riegler, *Langmuir*, 1998, **14**, 5285; C. Merkl, T. Pfohl and H. Riegler, *Phys. Rev. Lett.*, 1997, **79**, 4625; T. Pfohl and H. Riegler, *Phys. Rev. Lett.*, 1999, **82**, 783.
42 For an example of a CdTe-SEC see: D. G. Kurth, P. Lehmann and C. Lesser, *Chem. Commun.*, 2000, 949.